






Discovery of a Pulse-phase-transient Cyclotron Line in the X-Ray pulsar GRO J2058+42

S. Molkov¹ , A. Lutovinov^{1,2} , S. Tsygankov^{1,3} , I. Mereminskiy¹, and A. Mushtukov^{1,4,5}

¹ Space Research Institute, Russian Academy of Sciences, Profsoyuznaya 84/32, 117997 Moscow, Russia; molkov@iki.rssi.ru

² Moscow Institute of Physics and Technology, Moscow region, 141701 Dolgoprudnyi, Russia

³ Department of Physics and Astronomy, FI-20014 University of Turku, Finland

⁴ Leiden Observatory, Leiden University, NL-2300RA Leiden, The Netherlands

⁵ Pulkovo Observatory, Russian Academy of Sciences, Saint Petersburg 196140, Russia

Received 2019 August 6; revised 2019 August 24; accepted 2019 August 26; published 2019 September 18

Abstract

We report the discovery of absorption features in the X-ray spectrum of the transient X-ray pulsar GRO J2058+42. The features are detected around ~ 10 , ~ 20 , and ~ 30 keV in both *NuSTAR* observations carried out during the source type II outburst in spring 2019. The most intriguing property is that the deficit of photons around these energies is registered only in the narrow phase interval covering around 10% of the pulsar spin period. We interpret these absorption lines as a cyclotron resonant scattering line (fundamental) and two higher harmonics. The measured energy allow us to estimate the magnetic field strength of the neutron star as $\sim 10^{12}$ G.

Unified Astronomy Thesaurus concepts: X-ray binary stars (1811); Binary pulsars (153); Neutron stars (1108)

1. Introduction

GRO J2058+42 is a slowly rotating ($P_{\text{spin}} \simeq 196$ s) transient X-ray pulsar (XRP) discovered with the Burst and Transient Source Experiment (BATSE) on board the *Compton Gamma-Ray Observatory* (*CGRO*) during a type II (giant) outburst in 1995 September (Wilson et al. 1995). After this outburst a dozen normal ones (type I) had been observed during the next two years with *CGRO* and the *Rossi X-Ray Timing Explorer* (*RXTE*). These type I outbursts were spaced by about 110 day intervals, which was interpreted as an orbital period of the system (Wilson et al. 1996; Bildsten et al. 1997). At the same time additional short and weak outbursts were detected by BATSE halfway between these type I outbursts (Wilson et al. 1998). Combining these measurements with ones carried out with the All-Sky Monitor on board the *RXTE* observatory on an alternative orbital period of ~ 55 days was also considered (Wilson et al. 1998, 2005).

The source localization accuracy ($30' \times 60'$), obtained with the *CGRO* (Grove 1995) and subsequently restricted down to $4'$ with *RXTE* (Wilson et al. 1996), did not allow us to make an immediate determination of the optical counterpart. Only after the identification of GRO J2058+42 with the *Chandra* source CXOU J205847.5+414637 and following observations in the optical band was the normal companion reliably recognized as a Be star at a distance of 9.0 ± 1.3 kpc (Wilson et al. 2005).

Spectral properties of the source are poorly known. They were briefly reported and discussed by Wilson et al. (2000, 2005) using the *RXTE*/Proportional Counter Array (PCA) and *Chandra* data and by Krimm et al. (2008) based on the *Swift* X-Ray Telescope (XRT) data. These authors used an absorbed power law to describe the source spectrum in soft X-rays and the bremsstrahlung model in a wider energy band.

In this Letter we perform a detailed spectral analysis of GRO J2058+42 and report the discovery of the cyclotron absorption line in its spectrum with the *Nuclear Spectroscopic Telescope Array* (*NuSTAR*) observatory during the type II outburst in the spring of 2019. For the first time for accreting XRP such a feature is robustly detected only in the narrow range of pulse phases.

2. Observations and Data Reduction

Since its discovery in 1995 during the giant outburst and subsequent two years of activity, GRO J2058+42 remained in a quiet state until 2019. Only one weak type I outburst was detected in 2008 May (Krimm et al. 2008). The beginning of new type II outburst was registered with the *Neil Gehrels Swift Observatory* (Gehrels et al. 2004) on 2019 March 22 (Barthelmy et al. 2019) and later confirmed by the detection of the pulsed emission (Malacaria et al. 2019) with the Gamma-ray Burst Monitor (GBM; Meegan et al. 2009) on board the *Fermi* observatory.

This outburst lasted more than 100 days and was monitored by several X-ray instruments. To trace the source light curve we used available data from the *Swift*/Burst Alert Telescope (BAT; Krimm et al. 2013) in the 15–50 keV energy band (Figure 1).⁶ The *Swift*/BAT data have a gap around the outburst maximum; therefore, to better demonstrate an entire morphology of the outburst we used data of the *Fermi*/GBM⁷ that were aligned with the BAT ones at the moment of the second *NuSTAR* observation. Both light curves are in a good agreement with each other (Figure 1).

We also used data from the *Swift*/XRT (Burrows et al. 2005) to trace the evolution of the source flux in the soft energy band. The fluxes measured with XRT in the 1–10 keV energy range are shown in Figure 1 by red open circles. They were calculated from the source spectra obtained with the online tools (Evans et al. 2009), provided by the UK Swift Science Data Center.⁸

The *NuSTAR* observatory consists of two identical X-ray telescope modules, referred to as FPMA and FPMB (Harrison et al. 2013). It provides X-ray imaging, spectroscopy, and timing in the energy range of 3–79 keV with an angular resolution of $18''$ (FWHM) and spectral resolution of 400 eV (FWHM) at 10 keV. *NuSTAR* performed two observations of GRO J2058+42 on 2019 March 25 (ObsID: 90501313002) and 2019 April 11 (ObsID: 90501313004) with the on-source

⁶ <https://swift.gsfc.nasa.gov/results/transients/weak/GROJ2058p42>

⁷ <https://gammaray.msfc.nasa.gov/gbm/science/pulsars/lightcurves/groj2058.html>

⁸ http://www.swift.ac.uk/user_objects/

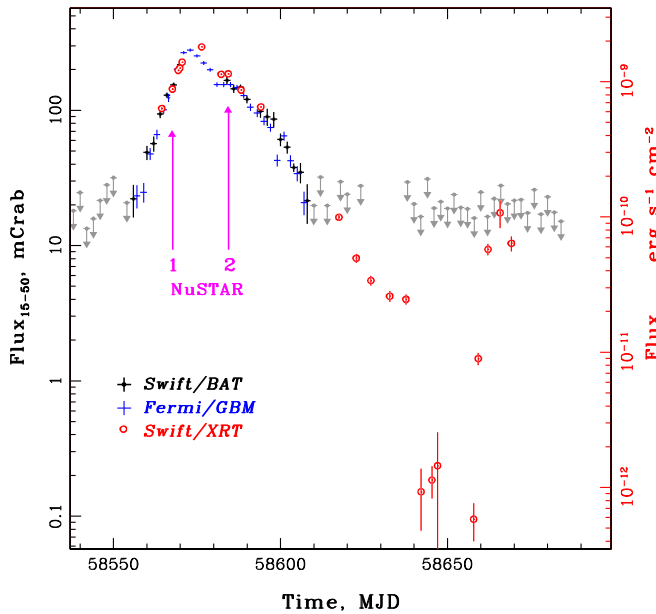


Figure 1. The *Swift*/BAT light curve (black crosses, 15–50 keV), *Fermi*/GBM pulsed emission (blue crosses, 12–50 keV), and *Swift*/XRT flux (red open circle, 1–10 keV) measured from GRO J2058+42 during the 2019 outburst. *Swift*/BAT data are in mCrab units (left axis), *Fermi*/GBM data are in $\text{keV cm}^{-2} \text{s}^{-1}$, and *Swift*/XRT data are in $\text{erg s}^{-1} \text{cm}^{-2}$ (right axis). To trace the outburst morphology XRT and GBM curves are aligned with the BAT one at the moment of the second *NuSTAR* observation. Dates of two *NuSTAR* observations are marked with vertical magenta arrows.

exposures of ~ 20 and ~ 40 ks, respectively. Note that both observations were carried out near the maximum of the outburst (see Figure 1, marked with the magenta arrows as “1” and “2”). The *NuSTAR* data were processed with the standard *NuSTAR* Data Analysis Software (NUSTARDAS) v1.8.0 provided under HEASOFT v6.25 with the CALDB version 20190513.

In the following spectral analysis we used the 4–79 keV energy band. An increase of the lower threshold energy from the standard 3–4 keV is due to both observations being made during the solar activity periods. It could affect the correctness of the background estimation with standard routines below 4 keV, where the background could be dominated by a few lines and the ~ 1 keV thermal plasma component, probably connected with reflected solar X-rays (Wik et al. 2014).

All obtained spectra were grouped to have at least 25 counts per bin using the GRPPHA tool. The final data analysis (timing and spectral) was performed with the HEASOFT 6.25 software package. All uncertainties are quoted at the 90% confidence level, if not stated otherwise.

3. Results

We performed a complete timing and spectral (including pulse-phase-resolved) analysis for both *NuSTAR* observations. Resulting spectra and pulse profiles of the source are very similar each other and for brevity we present most of following figures only for the first observation.

3.1. Energy-resolved Pulse Profile

Orbital ephemerides for GRO J2058+42 are unknown; therefore, the pulsating signal was searched only in barycentered light curves. Pulsations were clearly detected with high

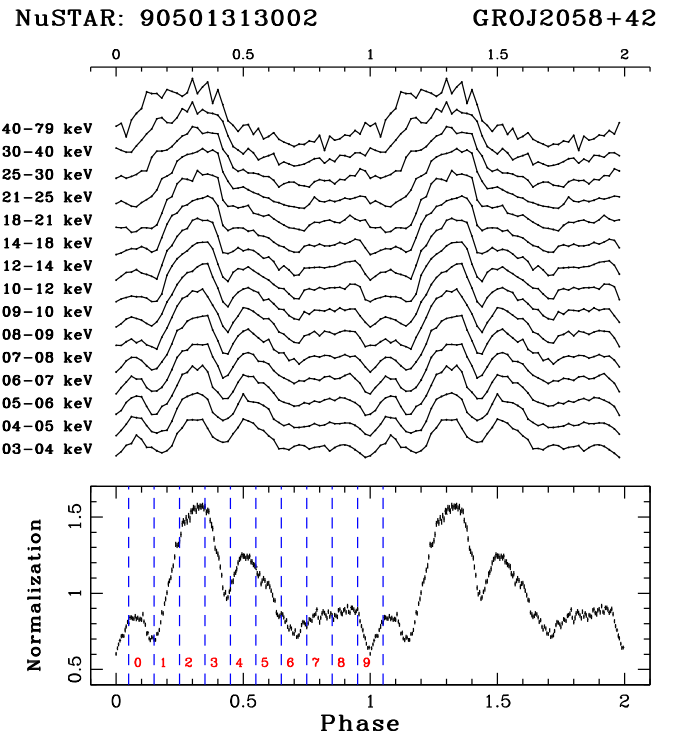


Figure 2. Energy-resolved pulse profiles of GRO J2058+42 obtained with *NuSTAR* in the first observation. In the bottom panel an averaged pulse profile is shown. Vertical lines demonstrate phase bins selected for spectral analysis.

significance at periods of 195.240(2) and 194.149(1) s for the first and second *NuSTAR* observations, respectively. These values were used in the subsequent analysis to fold light curves and for the pulse-phase-resolved spectroscopy.

Figure 2 presents energy-resolved pulse profiles of the source obtained in the first *NuSTAR* observation. We attributed phase 0 to the minimum of the folded light curve in the full instrument energy band. The pulse profile is clearly evolving with the energy.

At the few to about 10 keV energy range, the profile shows three distinct peaks at phases 0.1, 0.3, and 0.5. As the energy increases the two “outer” peaks disappear and the central peak eventually expands, while its minimum shifts to the phase ~ 0.7 .

The pulsed fraction gradually increases with the energy from $\sim 40\%$ at 3–5 keV to $\sim 60\%$ at 50–70 keV, which is observed for the majority of bright XRP (see, e.g., Lutovinov & Tsygankov 2009).

3.2. Phase-averaged Spectrum

The spectrum of GRO J2058+42 has a typical shape for accreting XRP (see, e.g., Nagase 1989; Filippova et al. 2005) and demonstrates an exponential cutoff at high energies (Figure 3(a)) that, e.g., can be explained in terms of the Comptonization processes in hot emission regions (see, e.g., Sunyaev & Titarchuk 1980; Meszaros & Nagel 1985). Therefore, at the first stage it was approximated with several commonly used models: a power law with an exponential cutoff (`cutoffpl` in the XSPEC package), a power law with a high-energy cutoff (`powerlaw*highcut`), and a thermal Comptonization (`comptt`). To take into account the uncertainty in the calibrations of two modules of *NuSTAR* the cross-calibration constant C between them was included in all spectral fits. It was found that the Comptonization model (Titarchuk 1994) with an inclusion of the iron emission line at 6.4 keV in the form of the Gaussian profile describes the

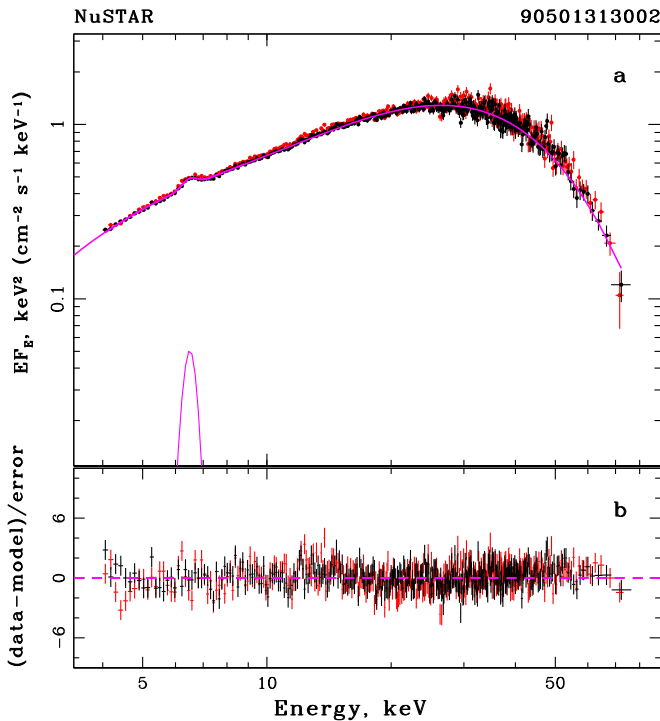


Figure 3. (a) Broadband energy spectrum of GRO J2058+42 obtained in the first *NuSTAR* observation. Black and red crosses correspond to FPMA and FPMB modules. Blue solid line represents the best-fit model (see details in the text). (b) Residuals from the best-fit model.

GRO J2058+42 spectrum significantly better than other models ($\chi^2 = 2255$ for 2117 degrees of freedom (dof) in a comparison with 3730 (2120 dof) and 3911 (2119 dof) for the first two models). Results of the approximation of the source spectrum obtained in the first *NuSTAR* observation with this model are show in Figure 3(a). Best-fit parameters are as follows: the seed photon temperature $kT_0 = 1.55 \pm 0.15$ keV, the plasma temperature $kT = 10.25 \pm 0.04$ keV, the plasma optical depth $\tau = 5.02 \pm 0.03$, the iron line energy $E_{\text{Fe}} = 6.48 \pm 0.03$ keV, the iron line width $\sigma_{\text{Fe}} = 0.24 \pm 0.03$ keV, its equivalent width $\text{EW}_{\text{Fe}} = 70 \pm 9$ eV, and the total flux in the 4–79 keV energy range $F_{4-79} \simeq 3.6 \times 10^{-9}$ erg s $^{-1}$ cm $^{-2}$. From the bottom panel (Figure 3(b)) it is seen that this model describes the spectrum adequately, and no obvious additional components are required. Note that it is difficult to compare directly the results of our measurements with ones obtained earlier (Wilson et al. 2005; Krimm et al. 2008), as the source was observed in different intensity states in different energy bands. Nevertheless, if we are restricted to only soft X-rays (<10 keV) and use the power-law model its parameters will be comparable with previously reported results.

The second *NuSTAR* observation was performed at the decaying part of the outburst (Figure 1) at a similar source intensity to the first one, $F_{4-79} \simeq 4.3 \times 10^{-9}$ erg s $^{-1}$ cm $^{-2}$. Spectral parameters measured in this observation agree well with those reported above, and again no additional components are required to describe the source spectrum.

3.3. Pulse-phase-resolved Spectroscopy

It is well established that spectra of XRP are significantly variable with the pulse phase. Parameters of the cyclotron resonant scattering features (CRSFs), if they are present in the spectra, also change (see, e.g., Burderi et al. 2000; Heindl et al. 2004; Kreykenbohm et al. 2004; Lutovinov et al. 2015 and references

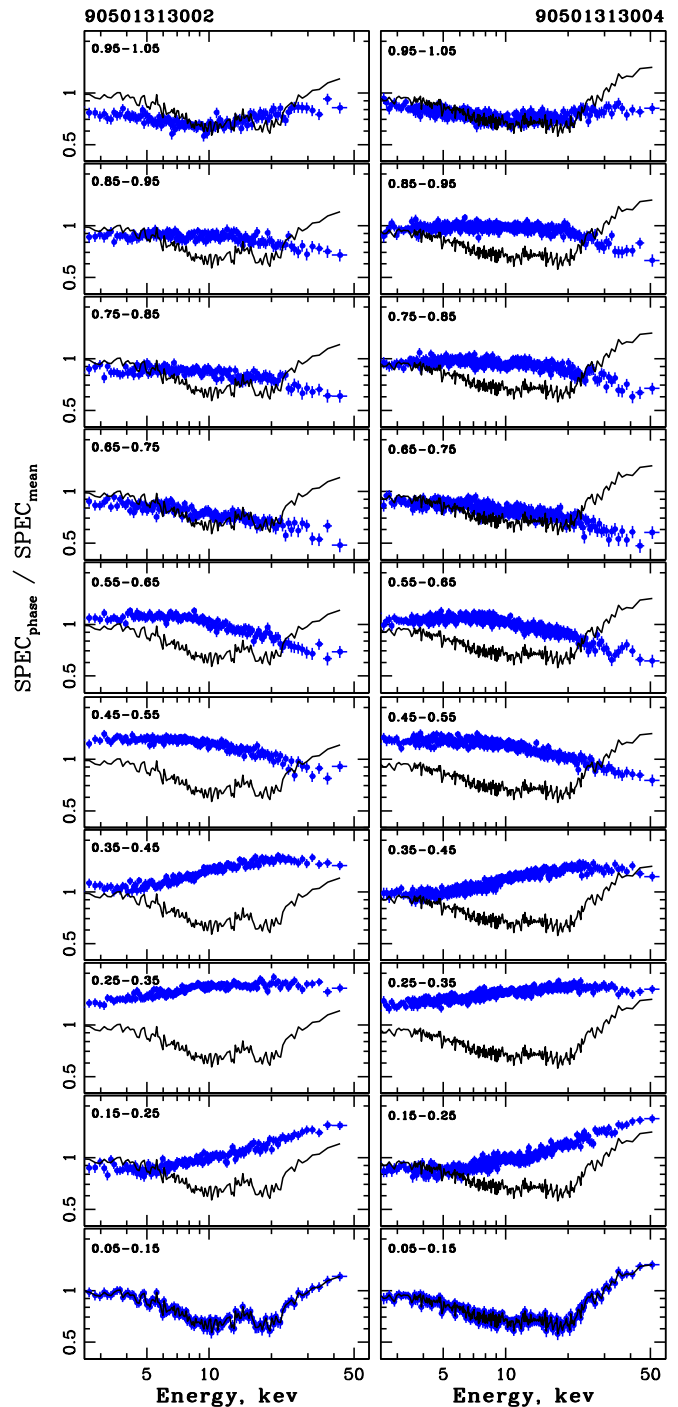


Figure 4. Ratio of the source spectra, measured at a given phase, to the averaged one (blue points) for two *NuSTAR* observations of GRO J2058+42 (left panels correspond to observation 1, right ones to observation 2). For comparison, the ratio at the phase 0.05–0.15 is shown in each panel with thin black lines.

therein). Therefore, the pulse-phase-resolved spectroscopy can be considered as a tool for the diagnosis of the geometry of the emission regions in the vicinity of the neutron star and its magnetic field structure. To trace an evolution of the GRO J2058+42 spectrum with the pulse phase we used the ratio of each phase’s spectrum to the pulsed-averaged one. It is important to note that the result of such an approach does not depend on the specific spectral model.

Results of the analysis are shown in Figure 4. It is clearly seen that the source spectrum varies significantly with the pulse

Table 1
Fit Parameters of the Cyclotron Absorption Line

ObsID	E_c , (keV)	σ_c , (keV)	τ_c
90501313002	$10.00^{+0.27}_{-0.61}$	$2.63^{+0.99}_{-0.38}$	$0.34^{+0.51}_{-0.10}$
	$19.47^{+0.22}_{-0.52}$	$3.23^{+0.39}_{-0.44}$	$0.42^{+0.14}_{-0.08}$
	$28.23^{+1.00}_{-2.43}$	$2.11^{+2.75}_{-0.87}$	$0.12^{+0.21}_{-0.07}$
90501313004	$10.91^{+0.62}_{-0.48}$	$3.14^{+2.18}_{-0.61}$	$0.24^{+0.43}_{-0.08}$
	$19.40^{+0.42}_{-0.44}$	$3.33^{+0.52}_{-0.54}$	$0.49^{+0.09}_{-0.14}$
	$28.31^{+0.97}_{-1.93}$	$3.40^{+1.70}_{-0.90}$	$0.18^{+0.16}_{-0.07}$

phase, primarily demonstrating an evolution of its hardness. In particular, the spectrum is hardest at the phases of 0.95–0.25 where the small interpeak is observed (see Figure 2). The spectra become gradually softer to the maximum of the first peak and to the second peak (phases 0.45–0.55) and return to the hard state further. It is important to note that such behavior is identical for both observations (Figure 4).

The most exceptional spectra are registered at phases of 0.05–0.15 in both observations, where an obvious deficit of photons around ~ 10 and ~ 20 keV is observed (Figures 4 and 5(a)). To quantify these features the spectrum from the first *NuSTAR* observation was fitted with different models. First of all we used the simplest model to adequately describe the averaged spectrum (`comptt+gaus`), resulting in an unacceptable fit with $\chi^2 = 1449.6$ for 1127 dof and obvious residuals around ~ 10 and ~ 20 keV (Figure 5(b)). The successive inclusion of additional CRSF components in the form of the `gabs` model significantly improves the fit quality: up to $\chi^2 = 1310.1$ (1124 dof) with the line around ~ 10 keV (Figure 5(c)) and up to $\chi^2 = 1103.0$ (1121 dof) with two lines at ~ 10 and ~ 20 keV (Figure 5(d)). Moreover, there is a marginal hint for the presence of an additional weak absorption feature around ~ 30 keV (Figure 5(e), fit quality is $\chi^2 = 1094.6$ for 1118 dof).

Similar absorption features at the same energies also are registered in the source spectrum reconstructed for the same pulse phases in the second *NuSTAR* observation, but in this case an additional third absorption line at ~ 30 keV improves the fit more significantly, from $\chi^2 = 1584$ (1531 dof) to $\chi^2 = 1547.8$ (1528 dof).

We interpreted these features as a cyclotron absorption line at ~ 10 keV with two higher harmonics, with parameters that can be summarized as in Table 1. E_c , σ_c , and τ_c are the energy, width, and optical depth of the cyclotron line and its higher harmonics.

To estimate the detection significance for each absorption feature we performed three 10^4 Monte Carlo simulations of the source spectra, successively adding the first, second, and third `gabs` components. We found that for the first observation the probabilities of a chance occurrence of 10, 20, and 30 keV features are $<10^{-4}$, $<10^{-4}$, and 0.1145, respectively. For the second observation corresponding probabilities are $<10^{-4}$, $<10^{-4}$, and 10^{-4} . Taking into account that the lines are registered independently in two observations at the same energies, the joint probabilities that they originate by chance are significantly lower.

We made a detailed search for any absorption features in spectra at other pulse phases, but all of them can be well described with the simple model, used for averaged spectra, and no additional absorption lines are required. To increase statistics we also constructed the spectrum averaged over all phases with the exception of data at phases 0.05–0.15, and

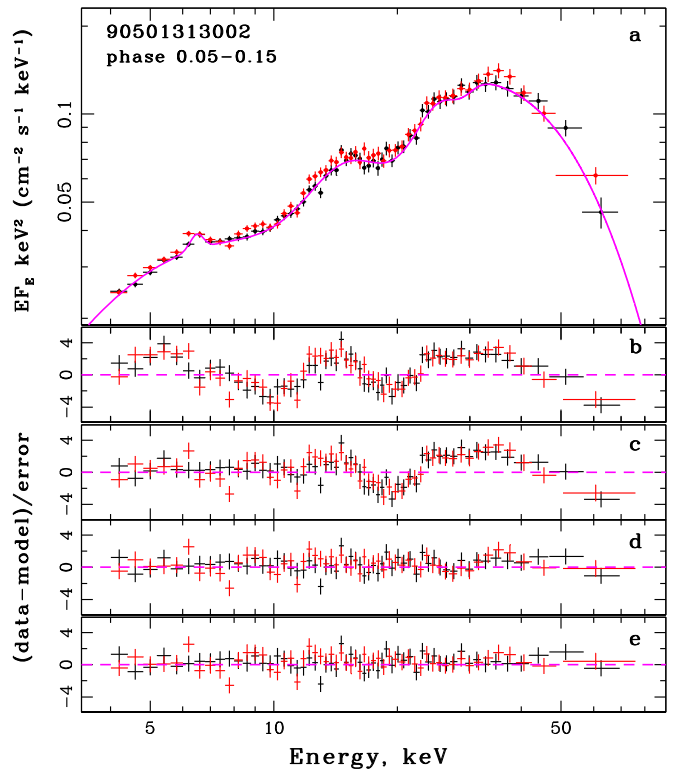


Figure 5. Energy spectrum of GRO J2058+42 at the pulse phases 0.05–0.15 for the first *NuSTAR* observation. The data from both the FPMA and FPMB modules are shown by black and red points, respectively. Residuals in the bottom panels demonstrate the quality of fits with four different models (see the text for details).

again we found no indication of the presence of absorption lines in this spectrum.

4. Discussion and Conclusions

Here we present the first robust detection of the CRSF localized in a very narrow range of the spin phases of GRO J2058+42 and covering only $\sim 10\%$ of the entire spin period. Previous evidence of a similar transient CRSF, detectable in a small fraction of the pulsar rotation, was revealed in spectra of several isolated neutron stars (see, e.g., Borghese et al. 2015). However, in the classical XRPs only a hint of the marginal detection of such a feature was reported for EXO 2030+375 based on the *INTEGRAL* data (Klochkov et al. 2008).

To explain the peculiar spectral properties of GRO J2058+42 one can consider a geometrical configuration of the system.

High mass accretion rates onto the surface of neutron stars in XRPs result in the appearance of accretion columns confined by a strong magnetic field of the neutron star and supported by a high internal radiation pressure (Basko & Sunyaev 1976; Wang & Frank 1981; Mushtukov et al. 2015). Thus, the cyclotron line can originate from the accretion column (Nishimura 2014, 2015; Schönherr et al. 2014) or it can be a result of the reflection of X-rays from the atmosphere of the neutron star (Poutanen et al. 2013; Lutovinov et al. 2015). Due to a large gradient of the B -field strength over the visible column height (see, e.g., Nishimura 2015) or latitudes on the stellar surface, the scattering feature can vanish from the observed energy spectra. However, a situation where the

accretion column is partially eclipsed by the neutron star at certain phases of the pulse and the observer sees only a fraction of the accretion column is possible (Mushtukov et al. 2018). In this case, the dispersion of the magnetic field strength over the visible part of the column is relatively small, and the cyclotron line can appear at some phases of pulsations as it is observed in GRO J2058+42.

It is also necessary to note that the visibility of both the neutron star surface and accretion column is strongly affected by the effects of gravitational light bending (see, e.g., Riffert & Meszaros 1988; Kraus 2001; Mushtukov et al. 2018). Remarkably, the column located on the opposite side of the neutron star tends to provide the majority of the observed X-ray energy flux due to effects of the gravitational lensing. In general, the pulse profile and spectrum of XRPs at supercritical luminosities are determined by a large number of factors including the accretion column height, compactness of the central object, angular distribution of initial X-ray photons at the stellar surface, edges of accretion column, etc. All of these factors have to be included in an accurate theoretical model.

Considering the $E_c \simeq 10$ keV feature as a fundamental energy of the cyclotron absorption line, the magnetic field in the emission region can be estimated as $B \sim 10^{12}$ G.

Another independent way to estimate the magnetic field of the neutron star is to consider its quiescent luminosity and long-term flux behavior. In particular, it was shown that the transition to the so-called propeller regime (Illarionov & Sunyaev 1975), when the rotating magnetosphere centrifugally inhibits the accretion process, can be used to determine a dipole component of the magnetic field of the neutron star (Tsygankov et al. 2016a, 2016b; Lutovinov et al. 2017). After the transition to the propeller regime the source spectrum becomes much softer with the blackbody temperature of ~ 0.5 keV and quiescent luminosity of $\sim 10^{33}$ erg s $^{-1}$ (Tsygankov et al. 2016a, 2017b; Wijnands & Degenaar 2016). However, as was shown later by Tsygankov et al. (2017a), a transition to the propeller regime is possible only for relatively fast spinning XRPs ($P_{\text{spin}} \lesssim 10$ s). In the slowly rotating pulsars (like GRO J2058+42) the accretion disk switches to the “cold” low-ionization state maintaining a stable mass accretion rate around 10^{14-15} g s $^{-1}$. This rate depends on the inner radius of the disk (Tsygankov et al. 2017a) and therefore can be utilized to estimate the magnetic field in XRPs (Nabizadeh et al. 2019; Tsygankov et al. 2019). Note that an analogous physical mechanism was proposed earlier for cataclysmic variables (see, e.g., Lasota 2001).

As can be seen from Figure 1 GRO J2058+42 switched to the quiescent state around MJD 58640. This state is characterized by a stable low-level flux around 10^{-12} erg s $^{-1}$ cm $^{-2}$ that corresponds to the luminosity around 10^{34} erg s $^{-1}$, assuming a distance to the source of 9 kpc. It is worth noting that a serendipitous *Chandra* detection of the source on 2004 February 24 resulted in the same flux, pointing to the quiescent nature of this emission. Important information about the emission mechanism can be derived from the spectral analysis in the quiescent state; however, available data do not allow us to robustly discriminate between the soft blackbody-like and hard accretion-like spectral models. However, as discussed above, this luminosity is too high for the propeller regime and can be interpreted as a stable accretion from the cold disk. In this case we can use Equation (7) from Tsygankov et al. (2017a) to estimate the magnetic field in the neutron star in

GRO J2058+42. Assuming a standard mass and radius of the neutron star and a source distance of 9 kpc, we get a magnetic field strength around $(1-2) \times 10^{12}$ G, which is in very good agreement with the value derived from the cyclotron energy.

We thank the *NuSTAR* and *Swift*/XRT teams for organizing prompt observations. This work was financially supported by the Russian Science Foundation (grant 19-12-00423).

ORCID iDs

S. Molkov  <https://orcid.org/0000-0002-5983-5788>

A. Lutovinov  <https://orcid.org/0000-0002-6255-9972>

S. Tsygankov  <https://orcid.org/0000-0002-9679-0793>

References

- Barthelmy, S. D., Evans, P. A., Gropp, J. D., et al. 2019, *GCN*, **23985**, 1
- Basko, M. M., & Sunyaev, R. A. 1976, *MNRAS*, **175**, 395
- Bildsten, L., Chakrabarty, D., Chiu, J., et al. 1997, *ApJS*, **113**, 367
- Borghese, A., Rea, N., Coti Zelati, F., Tiengo, A., & Turolla, R. 2015, *ApJL*, **807**, L20
- Burderi, L., Di Salvo, T., Robba, N. R., La Barbera, A., & Guainazzi, M. 2000, *ApJ*, **530**, 429
- Burrows, D. N., Hill, J. E., Nousek, J. A., et al. 2005, *SSRv*, **120**, 165
- Evans, P. A., Beardmore, A. P., Page, K. L., et al. 2009, *MNRAS*, **397**, 1177
- Filippova, E. V., Tsygankov, S. S., Lutovinov, A. A., & Sunyaev, R. A. 2005, *AstL*, **31**, 729
- Gehrels, N., Chincarini, G., Giommi, P., et al. 2004, *ApJ*, **611**, 1005
- Grove, J. E. 1995, *IAUC*, **6239**, 2
- Harrison, F. A., Craig, W. W., Christensen, F. E., et al. 2013, *ApJ*, **770**, 103
- Heindl, W. A., Rothschild, R. E., Coburn, W., et al. 2004, in *AIP Conf. Ser.* 714, *X-ray Timing 2003: Rossi and Beyond*, ed. P. Kaaret et al. (Melville, NY: AIP), **323**
- Illarionov, A. F., & Sunyaev, R. A. 1975, *A&A*, **39**, 185
- Klochkov, D., Santangelo, A., Staubert, R., & Ferrigno, C. 2008, *A&A*, **491**, 833
- Kraus, U. 2001, *ApJ*, **563**, 289
- Kreykenbohm, I., Wilms, J., Coburn, W., et al. 2004, *A&A*, **427**, 975
- Krimm, H. A., Barthelmy, S. D., Baumgartner, W., et al. 2008, *ATel*, **1516**, 1
- Krimm, H. A., Holland, S. T., Corbet, R. H. D., et al. 2013, *ApJS*, **209**, 14
- Lasota, J.-P. 2001, *NewAR*, **45**, 449
- Lutovinov, A. A., & Tsygankov, S. S. 2009, *AstL*, **35**, 433
- Lutovinov, A. A., Tsygankov, S. S., Krivonos, R. A., Molkov, S. V., & Poutanen, J. 2017, *ApJ*, **834**, 209
- Lutovinov, A. A., Tsygankov, S. S., Suleimanov, V. F., et al. 2015, *MNRAS*, **448**, 2175
- Malacaria, C., Jenke, P., Wilson-Hodge, C. A., & Roberts, O. J. 2019, *ATel*, **12614**, 1
- Meegan, C., Lichti, G., Bhat, P. N., et al. 2009, *ApJ*, **702**, 791
- Meszaros, P., & Nagel, W. 1985, *ApJ*, **299**, 138
- Mushtukov, A. A., Suleimanov, V. F., Tsygankov, S. S., & Poutanen, J. 2015, *MNRAS*, **454**, 2539
- Mushtukov, A. A., Verhagen, P. A., Tsygankov, S. S., et al. 2018, *MNRAS*, **474**, 5425
- Nabizadeh, A., Tsygankov, S. S., Karasev, D. I., et al. 2019, *A&A*, **622**, A198
- Nagase, F. 1989, *PASJ*, **41**, 1
- Nishimura, O. 2014, *ApJ*, **781**, 30
- Nishimura, O. 2015, *ApJ*, **807**, 164
- Poutanen, J., Mushtukov, A. A., Suleimanov, V. F., et al. 2013, *ApJ*, **777**, 115
- Riffert, H., & Meszaros, P. 1988, *ApJ*, **325**, 207
- Schönherr, G., Schwarm, F. W., Falkner, S., et al. 2014, *A&A*, **564**, L8
- Sunyaev, R. A., & Titarchuk, L. G. 1980, *A&A*, **500**, 167
- Titarchuk, L. 1994, *ApJ*, **434**, 570
- Tsygankov, S. S., Doroshenko, V., Mushtukov, A. E. A., Lutovinov, A. A., & Poutanen, J. 2019, *A&A*, **621**, A134
- Tsygankov, S. S., Lutovinov, A. A., Doroshenko, V., et al. 2016a, *A&A*, **593**, A16
- Tsygankov, S. S., Mushtukov, A. A., Suleimanov, V. F., et al. 2017a, *A&A*, **608**, A17
- Tsygankov, S. S., Mushtukov, A. A., Suleimanov, V. F., & Poutanen, J. 2016b, *MNRAS*, **457**, 1101

- Tsygankov, S. S., Wijnands, R., Lutovinov, A. A., Degenaar, N., & Poutanen, J. 2017b, [MNRAS](#), **470**, 126
- Wang, Y. M., & Frank, J. 1981, [A&A](#), **93**, 255
- Wijnands, R., & Degenaar, N. 2016, [MNRAS](#), **463**, L46
- Wik, D. R., Hornstrup, A., Molendi, S., et al. 2014, [ApJ](#), **792**, 48
- Wilson, C. A., Finger, M. H., Harmon, B. A., Chakrabarty, D., & Strohmayer, T. 1998, [ApJ](#), **499**, 820
- Wilson, C. A., Finger, M. H., & Scott, D. M. 2000, in [AIP Conf. Proc.](#) 510, The Fifth Compton Symposium, ed. M. L. McConnell & J. M. Ryan (Melville, NY: AIP), 208
- Wilson, C. A., Strohmayer, T., & Chakrabarty, D. 1996, [IAUC](#), **6514**, 2
- Wilson, C. A., Weisskopf, M. C., Finger, M. H., et al. 2005, [ApJ](#), **622**, 1024
- Wilson, C. A., Zhang, S. N., Finger, M. H., et al. 1995, [IAUC](#), **6238**, 1